Combustion and Flame 156 (2009) 14–24

Contents lists available at ScienceDirect

Combustion and Flame

www.elsevier.com/locate/combustflame

Interaction of the burning spherical droplets in oxygen-enriched turbulent environment

Chong Pyo Cho [a], Ho Young Kim [b,*], Sam S. Yoon [b]

[a] Automobile Energy & Environment Research Center, Korea Institute of Energy Research, 71-2 Jangdong, Yuseonggu, Daejeon, 305-343, Republic of Korea
[b] Department of Mechanical Engineering, Korea University, Anamdong, 5-Ga, Sungbukgu, Seoul, 136-701, Republic of Korea

ARTICLE INFO

Article history:
Received 3 April 2007
Received in revised form 30 September 2008
Accepted 3 October 2008
Available online 13 November 2008

Keywords:
Droplet interaction
Oxygen mole-fraction
Droplet inter-space distance

ABSTRACT

Three-dimensional numerical studies on the interaction of vaporizing and burning droplets were conducted to understand the burning characteristics of multiple droplets in a turbulent environment. The burning droplets characteristics, such as lifetime, surface temperature, vaporization, reaction, and burning rate were examined for various oxygen mole-fractions and geometrical arrangements of droplets. Results from a single droplet combustion test were first verified and validated against existing experimental data. Results indicate that turbulent intensity has a moderate effect on droplet burning rate, but not as prominent an effect as the oxygen mole-fraction. At high oxygen mole-fractions, droplet lifetime was short due to enhanced burning. It is shown that evaporation processes of multiple droplets are notably affected by the inter-space distance between droplets both in streamwise and spanwise directions. The burning rate as a function of oxygen mole-fraction and inter-space distance is determined and can be used as a guideline for future studies on spray combustion.

1. Introduction

Most numerical studies on the vaporization of a liquid droplet are conducted for laminar flow conditions, by assuming that the size of the eddy of an ambient turbulent flow is much larger than the droplet diameter and assuming that the flow near the droplet surface is laminar. On the other hand, if the turbulent eddy size is comparable to the droplet diameter, then the effects of both the turbulent intensity and length scale and of the free-stream mean velocity upon the drag coefficient and upon the overall heat and mass transfer become considerable. In many practical spray applications, the turbulence length scale of dissipative structures (Kolmogorov scale) is comparable to or smaller than the large droplet sizes, especially near the injector region [1]. Therefore, variations in the transport rates due to turbulence should be considered. Several relevant experimental studies showed weak turbulence effects on *single* droplet evaporation at room temperature [2–5]. These studies indicated that the ambient turbulence intensity does influence evaporation rates, although the effects of the turbulence length scale on the droplet evaporation rate were not prominent.

Although great experimental progress has been made in understanding the effects of turbulence on single-droplet evaporation, there have been few relevant numerical studies dealing with multiple droplets vaporization in hot turbulent flow. Unfortunately, burning of a single droplet is seldom observed in practical situations. Thus, insights on group combustion of *multiple* droplets of interest in real applications are needed.

There are two scenarios for group combustion. First, the change in heat and mass transfer due to the presence of neighboring droplets can generally be neglected if the spray is dilute; thus, single droplet physics should be suited to model burning of a diluted spray. However, in the second scenario of a dense spray, droplet interactions are sufficient to affect the physical properties of the gas in the region between droplets [6].

The multi-droplet combustion problem received much attention in the early 1980s and 1990s, particularly by Sirignano and his coworkers [7–10]. Tal et al. [7,8] calculated the gas flow field and the heat transfer between the hot stream and an array of axisymmetric droplets of equal size under laminar conditions. These simulations highlighted the vortices that form behind each droplet (or cylinder due to their 2D nature) and their periodic coherent structures; neither vaporization nor combustion of the droplets was considered in these studies. Subsequent investigations [9,10] considered vaporization and Hill's vortex of internal circulation of evaporating droplets placed in a laminar stream. Droplet combustion was not treated in Refs. [9,10]. For tractability, the computations were axisymmetric and thus precluded studies of geometrical variance or spanwise droplet inter-space distance. A fully 3D numerical code is needed to simulate droplet inter-space distance effects of the most general type.

The present numerical work is unique because it implements 3D modeling and takes into account turbulence for group com-

* Corresponding author. Fax: +82 2 929 3082.
E-mail address: kimhy@korea.ac.kr (H.Y. Kim).

0010-2180/$ – see front matter
doi:10.1016/j.combustflame.2008.10.026

Nomenclature

D	diffusion coefficient
d	droplet diameter
G_k	turbulence production term
h	enthalpy
I	turbulence intensity
k	thermal conductivity or turbulence kinetic energy
L	latent heat
l_k	Kolmogorov length scale
m	mass of droplet
$\dot{m}''$	mass flux
n	normal direction
r	droplet radius
T	temperature
t	time
u, v, w	gas velocity components
Y	species mass fraction
w_j	rate of mass production of the jth species per unit volume

Subscripts

d	droplet
F	fuel
g	gas phase
l	liquid phase
n	normal
ox	oxygen
t	tangential or turbulence
0	initial condition

Superscripts

*	dimensionless form
′	fluctuation

Greek symbols

ε	turbulence dissipation rate
η	general coordinate
μ	viscosity
ν	stoichiometric ratio
ρ	density

bustion of multiple droplets. Moreover, geometrical variations in both streamwise and spanwise directions can be investigated for burning droplets. This study also considers the effect of oxygen mole-fraction on multi-droplet burning, an effect that is important in oxygen-enriched combustion [11].

Combustion can be enhanced by increasing the oxygen mole-fraction. When the adiabatic equilibrium flame temperature is increased with higher oxygen concentration, heat transfer is enhanced and pollutant emissions such as soot can be reduced [11]. In spite of these benefits, there is limited understanding of oxygen-enriched spray combustion, especially when considered in light of interaction between burning liquid droplets. The objective of this study is to investigate vaporization and burning of multiple droplets in an oxygen-enriched turbulent flow. The inter-droplet distance and the ambient oxygen mole-fraction are chosen as major parameters. First, our numerical results are verified through a grid convergence check and by comparison with experimental data for a *single* droplet. To our knowledge, there are no data related to burning of multiple droplets in an oxygen-enriched turbulent environment. Thus, our numerical results can serve as benchmark data for future studies on multiple droplet combustion.

2. Model description

2.1. Governing equations for gas phase and liquid phase

In the physical configuration, sketched in Fig. 1, the liquid fuel droplets are exposed to a turbulent flow of high temperature and an oxygen-enriched environment. In this environment, they form a periodic array in the x, y, and z directions. It is assumed that buoyancy effects due to gravity are negligible when compared to the free stream convection. Also, the deformation of the liquid droplets can be neglected because the gas-based Weber number for the present study is smaller than unity [12].

Under these assumptions, the governing equations expressing the mass, momentum, energy, and species conservation for the gas and liquid phases can be expressed in the generalized form:

$$\frac{\partial}{\partial t}(\rho\varphi)+\frac{\partial}{\partial x_j}\left[\rho\left(v_j-\frac{\partial x_j}{\partial t}\right)\varphi\right]=\frac{\partial}{\partial x_j}\left(\Gamma_\varphi\frac{\partial\varphi}{\partial x_j}\right)+S_\varphi, \tag{1}$$

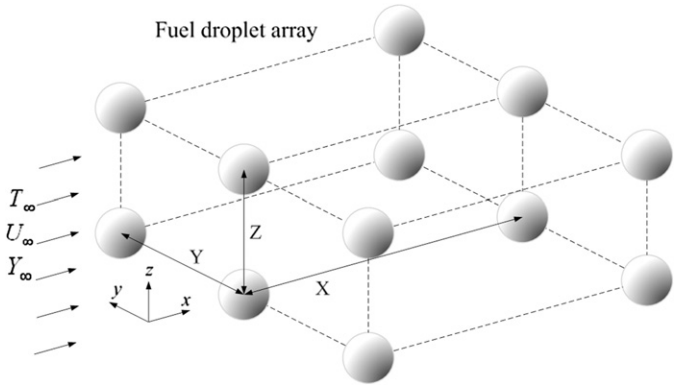

Fig. 1. Schematic of liquid fuel droplets burning in a turbulent flow.

Table 1
Generalized equations.[a]

Phase	Equation	φ	Γ_φ	S_φ
Gas phase	Continuity	1	0	0
	Momentum	v_i	μ_e	$-\frac{\partial p}{\partial x_i}+\frac{\partial}{\partial x_i}(\mu_e\frac{\partial v_j}{\partial x_i})$
	Turbulent kinetic energy	k	$\frac{\mu_e}{\sigma_k}$	$G_k-\rho\varepsilon$
	TKE dissipation rate	ε	$\frac{\mu_e}{\sigma_\varepsilon}$	$\frac{\varepsilon}{k}(c_1G_k-c_2\rho\varepsilon)$
	Species	Y_k	$\frac{\mu_e}{\sigma_Y}$	$-\nu_k w_k$
	Enthalpy	h	$\frac{\mu_e}{\sigma_h}$	$\sum h_{0k}\nu_k w_k$
Liquid phase	Continuity	1	0	0
	Momentum	v_i	μ_l	$-\frac{\partial p}{\partial x_i}+\frac{\partial}{\partial x_i}(\mu_l\frac{\partial v_j}{\partial x_i})$
	Energy	T	k	0

[a] $G_k=\mu_t(\frac{\partial v_i}{\partial x_j}+\frac{\partial v_j}{\partial x_i})\frac{\partial v_i}{\partial x_j}$, $\mu_e=\mu+\mu_t$, $\mu_t=\frac{\rho c_\mu k^2}{\varepsilon}$, $\sigma_k=\sigma_Y=\sigma_h=1.0$, $\sigma_\varepsilon=1.3$, $C_\mu=0.09$, $c_1=1.44$, $c_2=1.92$, $\varepsilon=C_\mu^{3/4}k^{3/2}/\ell$.

where φ, Γ_φ and S_φ are given in Table 1. The term, $\partial x_j/\partial t$, accounts for the conservation of mass during the variation of grid adjustment due to droplet evaporation. The droplet size is progressively reduced during evaporation.

The k–ε turbulence model is used to define the ambient turbulence structure for the gas phase. The governing equations using orthogonal coordinates were transformed into general curvilinear

coordinates. The Peng–Robinson equation [13] was used to represent the state of the gas surrounding the liquid droplets because of its suitability not only for an ideal gas, where the compressibility factor is unity, but also for a non-ideal gas, where the gas pressure is high (e.g., reaching critical pressure) and gas temperature is relatively low.

2.2. Turbulent combustion model for gas phase

Gas phase combustion, represented by the Eddy-Break-Up-Arrhenius (EBU-Arrhenius) model with finite-rate reactions, was applied to quantify the turbulent combustion rate of a heptane droplet. While the EBU model considers turbulent mixing, the Arrhenius model accommodates the kinetically controlled reactions. The reaction rate in a laminar flow is assumed to be a global single step reaction [14]. The reaction rate in the EBU-Arrhenius model is determined as follows [15]:

$$w_j = \min(w_{j,\mathrm{EBU}}, w_{j,\mathrm{Arr}}), \tag{2}$$

where

$$w_{j,\mathrm{EBU}} = C_\mathrm{R}\rho\frac{\varepsilon}{k}\min\left(Y_\mathrm{F}, \frac{Y_\mathrm{ox}}{\nu}\right), \tag{3}$$

$$w_{j,\mathrm{Arr}} = 2.87\times10^9\rho^{1.75}Y_\mathrm{F}^{0.25}Y_\mathrm{ox}^{1.5}\exp\left(-\frac{15098}{T}\right), \tag{4}$$

where C_R is an empirical constant, taken to be 4 according to Ref. [15]. The unit of Eqs. (2)–(4) is $(\mathrm{kg}/(\mathrm{s\,m^3}))$. In most cases, $w_{j,\mathrm{EBU}}$ is more often selected than $w_{j,\mathrm{Arr}}$ because the flow is dominated by mixing rather than chemical kinetics.

2.3. Interfacial boundary conditions

Boundary conditions at the liquid–gas phase are expressed as follows:

Continuity of tangential velocity and temperature

$$u_{\mathrm{t,l}} = u_{\mathrm{t,g}}, \quad T_\mathrm{g} = T_\mathrm{l}. \tag{5}$$

Shear stress balance

$$\mu_\mathrm{l}\left(\frac{\partial u_\mathrm{t}}{\partial n}\right)_\mathrm{l} = \mu_\mathrm{g}\left(\frac{\partial u_\mathrm{t}}{\partial n}\right)_\mathrm{g}. \tag{6}$$

Heat balance

$$\left(k\frac{\partial T}{\partial n}\right)_\mathrm{g} = \left(k\frac{\partial T}{\partial n}\right)_\mathrm{l} + \dot{m}''L. \tag{7}$$

Mass balance

$$\dot{m}'' = Y_\mathrm{F}\dot{m}'' - \rho_\mathrm{g}D_\mathrm{g}\left(\frac{dY_\mathrm{F}}{dn}\right), \quad \dot{m}'' = \rho_\mathrm{g}\left(u_n - \frac{dr}{dt}\right), \tag{8}$$

where the subscript t stands for the tangential component. Subscripts l and g represent the liquid and gas phases, respectively. The rate of radius change of a liquid droplet due to vaporization is obtained by considering the liquid density variation due to heat transfer from the hot gas to the droplet:

$$\dot{m} = -\int \dot{m}''\,dA = \frac{d}{dt}(\bar{\rho}_\mathrm{l}V) = \bar{\rho}_\mathrm{l}\frac{dV}{dt} + V\frac{d\bar{\rho}_\mathrm{l}}{dt}, \tag{9}$$

$$\frac{dr}{dt} = \left(\frac{1}{4\pi r^2}\frac{dm}{dt} - \frac{r}{3}\frac{d\bar{\rho}_\mathrm{l}}{dt}\right)\frac{1}{\bar{\rho}_\mathrm{l}}, \tag{10}$$

where $\bar{\rho}$ is the volume-averaged density varying at every time step due to the changing liquid temperature. The concept of film theory is employed to calculate the total mass flux of the gas mixture. The thermo-physical properties of each phase and the mixture are the same as those in our previous study [6].

2.4. Variation of adiabatic flame temperature with oxygen mole-fraction

The adiabatic flame temperature variations with the level of oxygen mole-fraction were calculated using the computer program HPFLAME [16], which is based on the equilibrium products of the combustion code [17]. HPFLAME provides the adiabatic flame temperature, equilibrium products, and mole fractions of the primary product species in adiabatic, constant-pressure combustion. When the oxygen mole-fraction in a gas varies, so does the adiabatic flame temperature because of the difference in the enthalpies of the reactants. The adiabatic flame temperature for various oxygen mole-fractions is found by curve-fitting the data obtained using the HPFLAME code.

2.5. Numerical method

The governing equations for the gas and liquid phases were discretized using a finite-volume method. The SIMPLEC algorithm [18] was applied to solve the gas and liquid flow fields, and the power-law scheme [19] was used for the convective and diffusive fluxes at the control volume surface. A fully implicit scheme was employed for the time marching calculation [19]. The discretized equations were solved with the Strongly Implicit Procedure (SIP) method [20]. The body-fitted grid system was generated by the elliptic differential equation technique, in which Poisson equations are solved to determine the values of the curvilinear coordinates in the physical space. In addition, the generated grid was made locally orthogonal to the droplet surface to facilitate the application of the boundary conditions. In addition, exponential stretching in the radial direction was used to enhance the resolution in the region near the body surface. Symmetry conditions were applied to the upper and lower boundaries of the computational domain to replicate the presence of neighboring droplets above and below the computational domain, respectively, as shown in Fig. 2. A grid of $371\times61\times61$ for the gas-phase flow and a grid of $61\times41\times61$ for the liquid-phase were employed, whose resolutions, based on grid sensitivity, were found to be acceptable, as shown in Fig. 3. The smallest grid size used was $\Delta\eta_{\min} = 0.01r(t)$, with a typical time step of $\Delta t = 0.01$ ms or less to satisfy the CFL condition and ensure numerical stability. Here, note that $r(t)$ is the droplet radius varying with time due to vaporization.

3. Results and discussions

3.1. Model validation

Prior to simulating droplet combustion, the three-dimensional code was first "verified" by calculating flow around a cylinder in a two dimensional configuration. Results obtained with the current code were compared with those described in Refs. [21–23]. The operating Reynolds number was $\mathrm{Re}_\mathrm{cyl} = UD/\nu = 40$, where D is the cylinder diameter (or $2r_0$). Here, the variation in wake size, streamwise inter-spacing distance, and location of the vortices (as well as the flow separation point in the recirculation region) were computed, as shown in Fig. 4 (this figure shows the actual computed streamlines). Comparisons indicate that the present code yields results with an error smaller than 4.2%, as shown in Table 2.

The second test case is that of a vaporizing spherical droplet, the diameter-squared history of a vaporizing decane droplet from Ref. [24] was compared to our numerical estimates. This reference provides the droplet size and the temperature history. The initial conditions of this experiment were $d_0 \approx 2$ mm and $T_{\mathrm{d},0} = 315$ K. The air stream temperature was $T_\mathrm{g} = 1000$ K and the initial Reynolds number was $\mathrm{Re}_{\mathrm{d},0} = 17$. Thermocouples placed inside

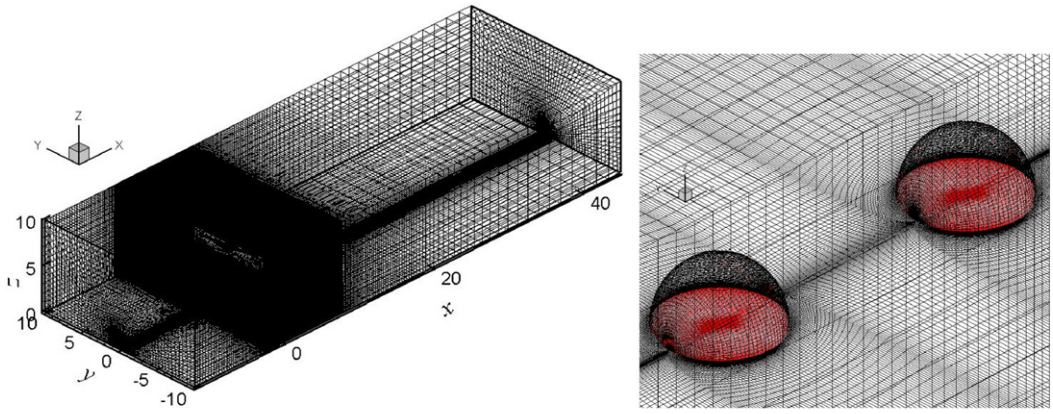

Fig. 2. Grid system for gas phase and droplet interior.

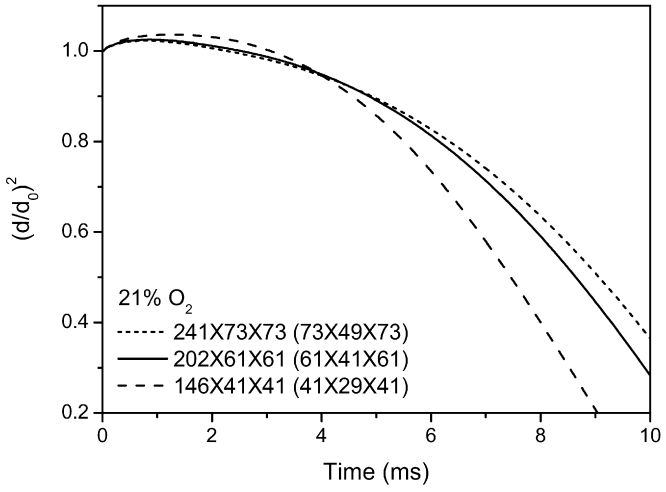

Fig. 3. Variation of diameter squared obtained from various numerical grids.

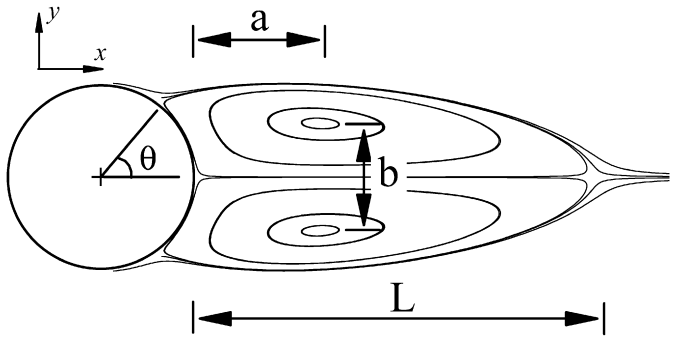

Fig. 4. Modeled streamlines for Re = 40 and definition of wake parameters.

Table 2
Model results compared to previous research for Re = 40.

	Constanceau and Bouard [21]	Rengel and Sphaier [22]	Wanderley and Levi [23]	Present study	Standard deviation
C_d	N.A.	1.61	1.60	1.65	0.022
L/D	2.13	2.23	2.10	2.16	0.048
a/D	0.76	0.72	0.69	0.69	0.029
b/D	0.59	0.58	0.58	0.59	0.005
θ	53.50	54.06	53.20	53.55	0.309

the suspended droplet were used to measure the droplet temperature evolution at various internal locations. Comparisons with the present calculations are provided in Fig. 5. The temperature inside the droplet measured at $r/r_0 = 0.6$, is compared with our numerical estimates in Fig. 5b. Good agreement with the experimental data is obtained and the droplet heat-up period is well retrieved featuring a diameter-squared is a nonlinear function of time (a fairly large portion of the entire lifetime).

3.2. Effect of oxygen mole-fraction on a single burning heptane droplet

The droplets initially at a temperature of 300 K were placed in a hot turbulent air stream at a pressure of 10 atm and a temperature $T_\infty = 1250$ K. The O_2 mole-fraction varied between 15% and 90%. Distances between droplets were $4r_0$ to $20r_0$ in the x-direction and $5r_0$ to $20r_0$ in the y- and z-directions. The initial Reynolds number, based on the droplet diameter ($d_0 = 100$ μm) and flow properties, was set to $\mathrm{Re} = U_\infty d_0/\nu = 50$ in all cases (except for the code-verification calculations described in the previous section). The droplet diameter (d_0) was the characteristic length and the free stream velocity was $U_\infty = 8.6$ m/s. According to Birouk and Gökalp [5], it is meaningless to use a characteristic or reference length (l_c) greater than the droplet diameter (i.e., $l_c/d_0 > 1$) because turbulence effects will not manifest themselves. In this paper, the turbulence effect on droplet evaporation was observed when the characteristic length was set to $l_c = 0.5d_0$ (or $l_c = r_0$).

The flow was nearly laminar at Re = 50, but artificially generated turbulence can be introduced even at low Reynolds numbers as indicated in Refs. [2–5] by directing free-stream flow through a wire mesh. Flow separates while passing through the mesh, which generates turbulent eddies or vortices. One of the objectives of this effort is to demonstrate that this model can replicate the physical scenario of induced turbulent flow in experiments at low Reynolds numbers.

As shown in Fig. 6, when the turbulence intensity is increased, the droplet vaporization rate also increases because of enhanced turbulent mixing. Here, dissipation rates assigned to turbulence intensities of $I = \sqrt{u'^2 + v'^2 + w'^2}/U_\infty = 0.01$, 0.1, 0.2, and 0.3 are $\varepsilon = 3.9$, 3866, 30925, and 104373 $\mathrm{m}^2/\mathrm{s}^3$, respectively. This trend agrees with the experiments carried out in Refs. [2–5] under weak natural convection. Note that the change in the characteristics length scale, l_c, for a fixed value of turbulence intensity does not influence the vaporization rate as much as the Kolmogorov length

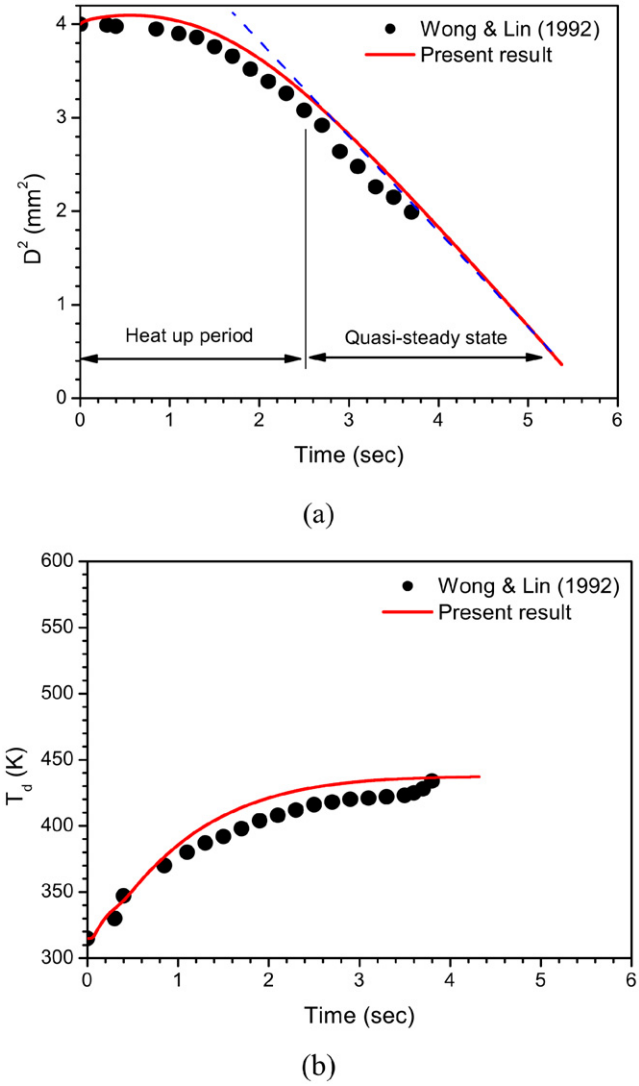

Fig. 5. Temporal variation of the (a) droplet diameter-squared and (b) the droplet temperature obtained at $r/r_0 = 0.6$ for decane.

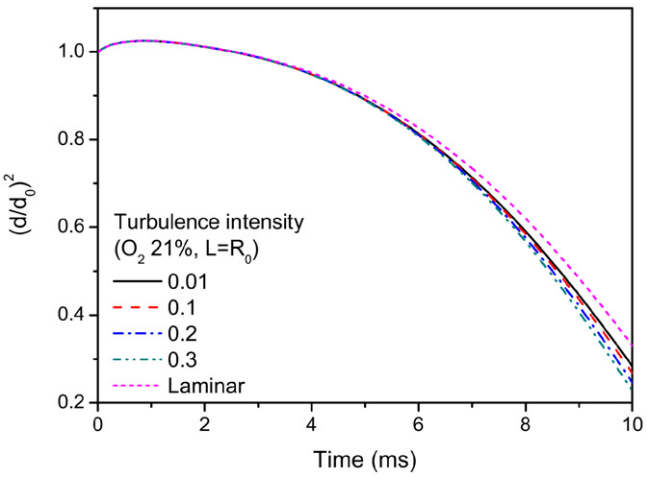

Fig. 6. Evolution of diameter-squared for a single liquid fuel droplet subject to various turbulence intensities.

scale, l_k, because the magnitude of l_k is predominantly determined by viscosity and turbulence intensity (or fluctuating velocity) while l_k is a weak function of l_c.

Table 3
Comparison of the model results with the data taken from Ref. [3].

	T_∞ (1 atm)	$T_{0,l}$	TI	Length scale	Lifetime
Experiment [3]	425 K	N.A.	0.14	0.5 mm or less	5.2 s
Model	425 K	300 K	0.14	0.25 mm	5.7 s

Although the trend of the present computational results was consistent with that of the experimental data from Refs. [2–5], the influence of turbulence intensity in our results is not as significant as that suggested by previous experimental studies. This is so because our results were obtained at extremely high gas temperatures ($T_\infty = 1250$ K) while experiments reported in Refs. [2–5] were carried out at a standard ambient temperature of $T_\infty \sim 300$ K. Since the gas temperature effect was dominant in our case, the turbulence intensity effect was commensurately obscured.

The gas temperature used in Ref. [3] was moderately high, $T_\infty = 425$ K, which we also used to quantitatively show the predictive capability of our code. Table 3 compares computational results to experimental data from [3]. Lifetime was within 8.8% subject to a turbulence intensity (TI) value of $I = 0.14$ for both modeling and experiment.

Note that all results shown hereafter are obtained at the low turbulence intensity of $I = 0.01$. Fig. 7 shows snapshots of temperature contours for the single droplet case at 15%, 50%, and 70% O_2 mole-fractions. At 15% O_2 mole-fraction, the core-flame (hottest spot) was located far downstream from the droplet. The system operates in the wake flame mode where heat is transferred primarily from the hot gas, generated by the flame to the droplet. Droplet evolution was similar to that found under pure vaporization without burning. As the O_2 mole-fraction increases, the flame approaches the droplet, as shown in Fig. 7b. With an O_2 mole-fraction of 50%, the flame is closer to the droplet, but the system continues to operate in the wake-flame mode. When the O_2 mole-fraction is further increased to 70% (see Fig. 7c), the system converts to a lateral flame mode where the flame partially surrounds the droplet and enhances heat transfer between the droplet surface and the flame thereby augmenting the vaporization rate.

When the O_2 mole-fraction is increased as shown in Fig. 8, the droplet's lifetime is reduced. The flame is situated closer to the droplet surface when O_2 increases and this accelerates the vaporization rate. Also, the heat-up period characterized by the nonlinear behavior of d^2 with time is shortened. Finally, ignition is faster and the flame region is more compact when the O_2 mole-fraction increases. For the liquid phase, the temperature isocontours inside the droplet correspond to those from Hill's vortex, which is driven by shear at the interface.

3.3. Heptane: Effects of streamwise inter-space distance (X)

Fig. 9 shows the flame configuration for multiple droplets at 4 ms. The O_2 mole-fraction is set to 15% and the streamwise distance between droplets, X, is set to $4r_0$ and $10r_0$ in Figs. 9a and 9b. For $X = 4$, the second droplet is affected by the low temperature of the unburned fuel vapor, which evolves from the first droplet. However, when X is increased ($X = 10$), the wake-flame of the first droplet induces a lateral flame around the second droplet enhancing the vapor release rate and yielding lateral and wake flames around the second droplet.

Figs. 10a and 10b show the temporal variation of the surface temperature and droplet size for different values of X. Note that the surface temperature is determined by averaging over the droplet surface. For the single and first droplet, there are two distinct heating phases: The first heating phase takes approximately 1 ms and then the rate of the temperature increase is slowed

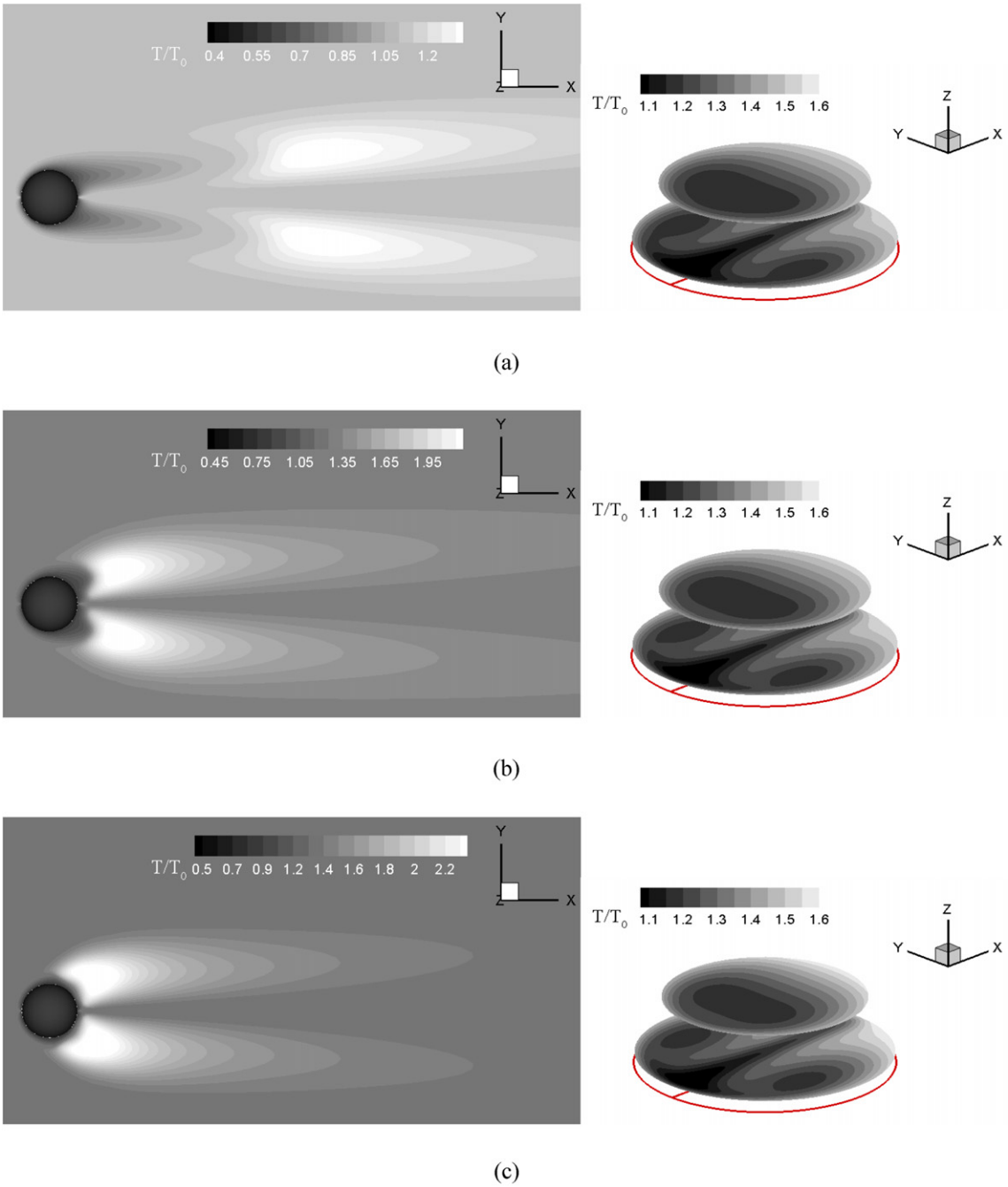

Fig. 7. Temperature contours of a single droplet for various O_2 mole-fractions at 3 ms. (a) Gas phase (left) and liquid phase (right) at 15% O_2, (b) gas phase (left) and liquid phase (right) at 50% O_2, (c) gas phase (left) and liquid phase (right) at 70% O_2.

by internal mixing between hot surface and the cold core of the droplet. Once this mixing between hot and cold is complete, the surface temperature increases again in the later period, eventually reaching the boiling point ($T_{b,heptane} = 475.5$ K at 10 atm), as shown in Fig. 10a. It is noteworthy that the droplet surface temperature fluctuates at a certain frequency after the rapid increase in the temperature. This fluctuation is caused by competition between flame heating, which increases the surface temperature, and the relatively low temperature of evaporated fuel vapors which cool the surface. The flame heating enhances evaporation by increasing fuel evaporation, which is manifested as an increase in the fuel mass flux, $\dot{m}''$, at the droplet surface [25,26]. However, the relatively low temperature evaporated fuel reduces the local surface temperature temporarily. Consequently, the fuel's evaporating rate is slowed down. The augmented temperature difference increases heat transfer from surrounding flames ultimately yielding the observed cyclic pattern shown in Fig. 10a.

The spanwise distances were purposely set to large values of $Y = Z = 20$ so that the first and second droplets could not be influenced by the presence of neighboring droplets along the y and z directions. Model results indicate that when X decreases, the surface temperature of the first droplet is hardly affected. According to Fig. 10a, however, as X decreases, the surface temperature of the second droplet is increased during the first 3.5 ms. Within this time period, as the second droplet approaches the first, the second droplet is less influenced by free-stream convection because of the screening effect of the first. As a result, Hill's vortex circulates less within the second droplet and, thus, the surface temperature

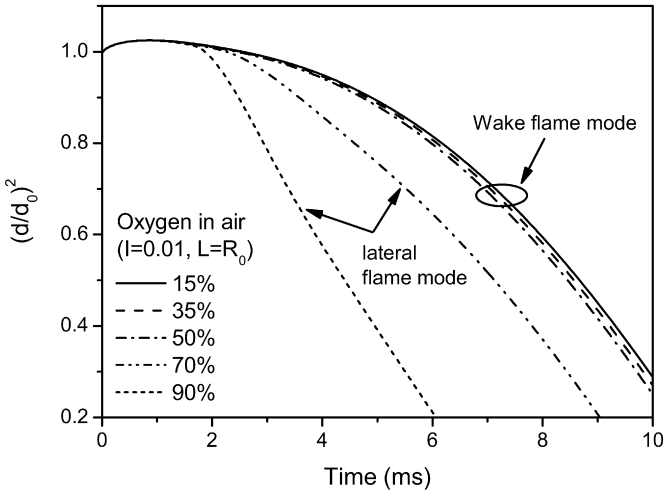

Fig. 8. Reduction in droplet diameter due to evaporation at various O_2 mole-fractions.

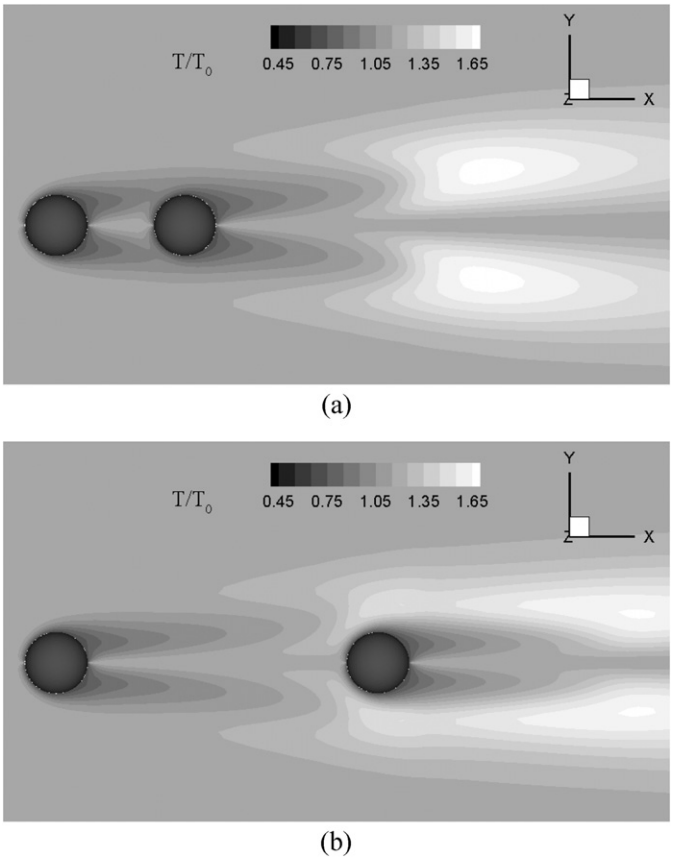

Fig. 9. Variation in gas temperature distribution due to change in X: (a) $X = 4$, (b) $X = 10$. The snapshots are taken at 4 ms for 15% O_2 with fixed $Y = Z = 20$.

is increased due to the reduced level of internal mixing with the relatively cold fluid inside the droplet.

After this mixing stage (for $t > 3.5$ ms), the second row of droplets located further downstream features higher surface temperature, because of the heat they receive from the first row. In this regime, due to the shorter distance X, the second droplet's temperature decreases because the low-temperature fuel vapor from the first droplet surrounds the second droplet.

An interesting behavior was observed when comparing results obtained for $X = 10$ and $X = 20$. According to Fig. 10b, the vaporization rates of the second droplet are higher than those of the first droplet, despite their decreased exposure to convection. This is because the second row of droplets receives extra heat from the wake-flame of the first droplet, but this wake-flame takes longer to reach the second droplet when $X = 20$ than when $X = 10$. This result is manifested in the surface temperature of the second droplet at $X = 10$ being greater than that for $X = 20$ until $t = 6$ ms as shown in Fig. 10a. Once the flame reaches the second droplet (i.e., $t > 6$ ms), the temperature for $X = 20$ overtakes that for $X = 10$ due to less shielding from convection, which increases the fuel vapor release rate and enhances combustion. This outcome is reflected in Fig. 10b, although there is a time lag for the increased temperature to be reflected in decreased diameter; that is, it takes about 2 ms ($t = 8$ ms) for the second droplet to respond to increased temperature, which eventually reduces the droplet size through evaporation.

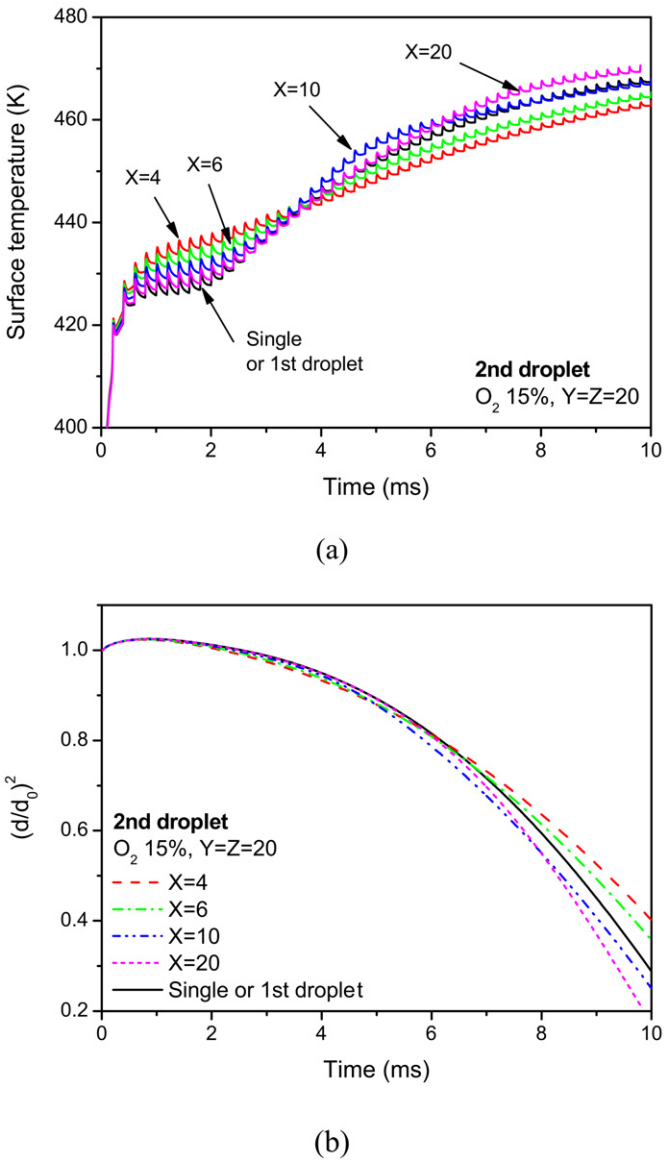

Fig. 10. Temporal variation of (a) surface temperature and (b) diameter squared of interacting droplets at 15% O_2 for various X with fixed $Y = Z = 20$.

In summary, four major effects compete in the relatively low ambient oxygen cases. First, convection-induced internal circulation (or Hill's vortex) temporarily decreases the droplet surface temperature due to the mixing with relatively cold fluid inside the droplet. Second, the first droplet shields the second droplet from

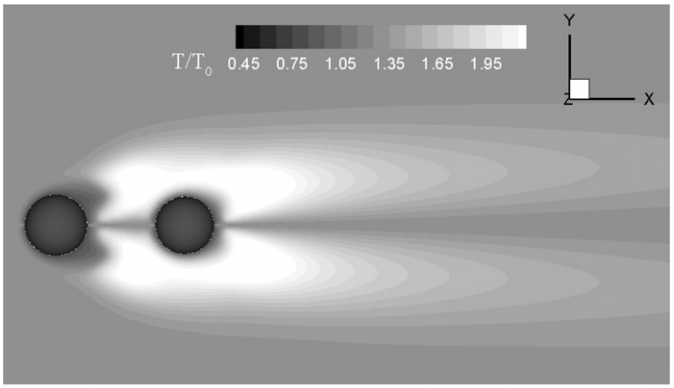

(a)

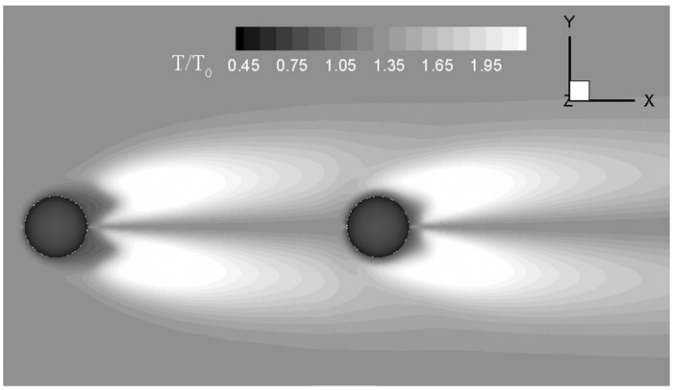

(b)

Fig. 11. Temperature contours of gas phase at 4 ms and 50% O_2 for different X with fixed $Y = Z = 20$: (a) $X = 4$, (b) $X = 10$.

convective effects while also providing relatively cool evaporating fuel. Third, the wake-flame of the first droplet can operate as a lateral flame and enhance evaporation from the second droplet. Fourth, the distance traveled by this wake-flame also affects the property of the second droplet.

As shown previously in Figs. 7b and 7c for the single droplet case, the flame configuration transitions from wake-flame mode to a lateral flame mode with increasing O_2 mole-fraction. The trend is consistent for multi-droplet cases where the lateral flame appears for all streamwise distance X when the O_2 mole-fraction exceeds 50% (see Fig. 11).

When $X = 4$, the individual flames appear in the early stage of burning and later merge, forming a single, surrounding flame as shown in Fig. 11a. Heat received by the second droplet is substantially increased because the second droplet is surrounded by the merged single flame. On the other hand, when $X = 10$, the lateral flame mode prevails for most of the droplet's lifetime, as shown in Fig. 11b.

This merged single flame at small inter-space distance controls the characteristics of the second droplet. With decreasing X, the surface temperature of the second droplet is increased, as shown in Fig. 12a. In this high O_2 mole-fraction case, rapid evaporation is shown in Fig. 12b. The nonlinear heat-up period is also shortened.

Other competing factors, such as the Hill's vortex, low temperature vapor of the first droplet, and convection shielding are less important in the high-O_2 mole-fraction case than for the low-O_2 mole-fraction case (i.e., 15%), because the merged single, surrounding flame plays a dominant role in defining the environment of the second droplet.

The dimensionless burning rates of the first and second droplets divided by the single spherical droplet burning rate (i.e., $\dot{M}^*_{1,2} = \dot{M}_{1,2}/\dot{M}_s$) are plotted with respect to X and O_2 mole fraction in

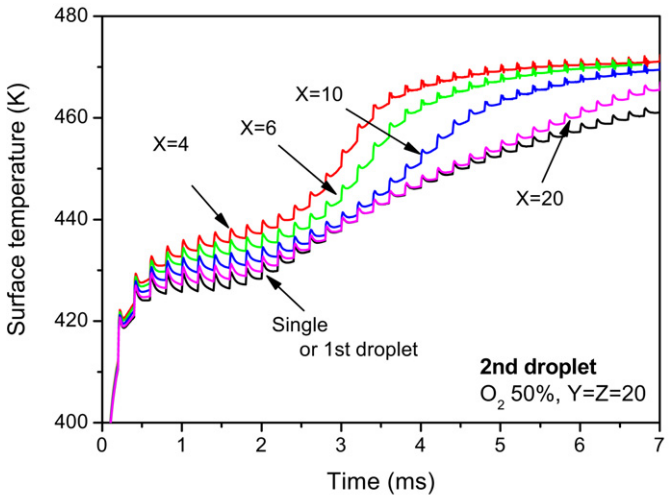

(a)

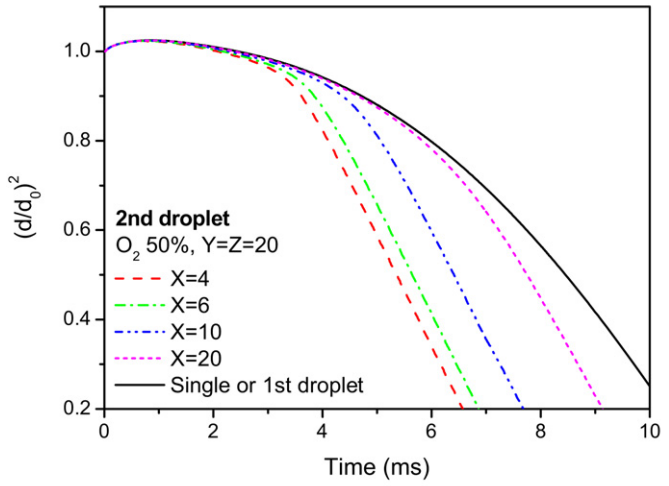

(b)

Fig. 12. Temporal variation of (a) surface temperature and (b) diameter squared of interacting droplets at 50% O_2 for various X with fixed $Y = Z = 20$.

Fig. 13. A "single" droplet is estimated by setting a large spanwise distance, i.e., $Y = Z = 25$ and results were obtained at "all" values of O_2 mole-fraction and are not a function of X for this comparison. The ratio is calculated when the initial droplet mass is reduced to 50% for the first droplet or to 10% for the second droplet.

When X increases, the maximum change of $\dot{M}^*_1$ lies within 3% (resulting in $\dot{M}^*_1 = 0.97$) for the first droplet at 70% O_2 mole-fraction, as shown in Fig. 13a. Differences are due to subtle changes in the flow field; note Y and Z are 20 in this case but they were equal to 25 for the single droplet case. Because less heat is available due to the distant location of the flame, evaporation of the first droplet is slightly reduced. When O_2 mole-fraction is less than 50%, the burning rate for the first droplet is the same as that for the single droplet. Overall, the change in the burning rate of the first droplet is relatively minor even at high oxygen mole-fraction because the change with respect to X and O_2 lies within 3%.

For the second droplet, $\dot{M}^*_2$ reaches 1.71 when X decreases at O_2 mole-fraction greater than 15%, as shown in Fig. 13b. With the closely located flame of the first droplet at high O_2 mole-fraction,

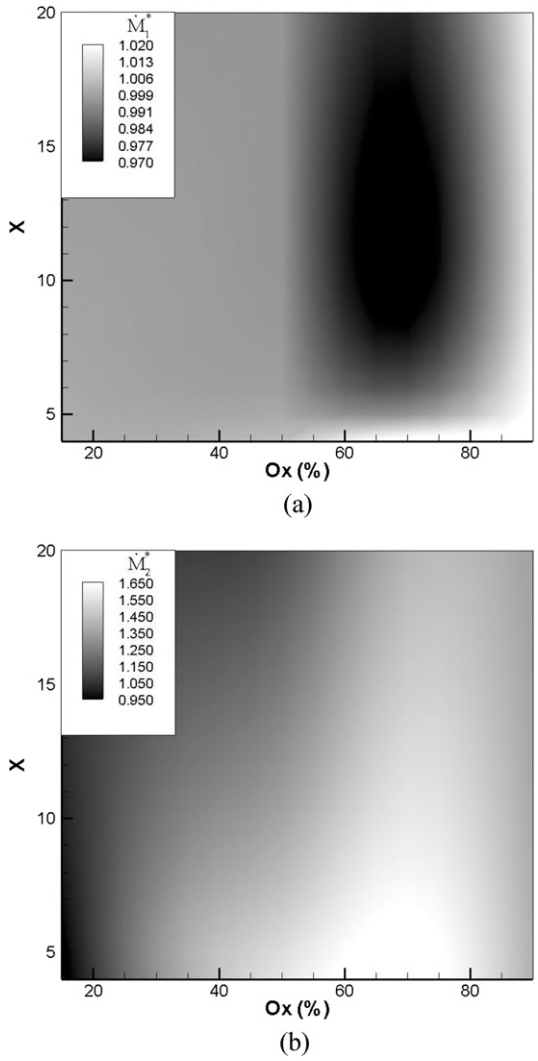

Fig. 13. Relative burning rate of interacting droplets to that of single droplet at $Y = Z = 20$: (a) 1st droplet, (b) 2nd droplet.

the burning rate is notably enhanced. However, this trend is reversed when O_2 mole-fraction is less than 15% for the reasons put forward to describe Fig. 10. Overall, the burning rate of the second droplet is strongly affected by the flame configuration characterized by O_2 mole-fraction and streamwise distance, X.

3.4. Heptane: Effect of the spanwise distance (Y and Z)

Effects of the spanwise distance on the droplet burning characteristics are examined in this section. Fig. 14 shows the flame configuration at 5 ms for 35% O_2 mole-fraction, a relatively large $X = 10$ and a small $Y = Z = 5$. The flames of the first droplets merge into a single flame, eventually yielding group combustion behavior. In this single flame mode, the heat flux to the second droplet is substantially increased because it is surrounded by the single flame. One may expect an accelerated flow at small $Y = Z = 5$, which in turn induces enhanced convection and rapid circulation or internal mixing of the second droplet. Furthermore, greater convection locates the first droplet flame closer to the front of the second droplet, inducing faster flame merging.

As expected, Fig. 15 quantitatively shows that the second droplet evaporates faster when Y and Z are reduced under greater convection inducing rapid flame merging. Note that the evaporation rate of the first droplet is hardly affected by the changing Y and Z.

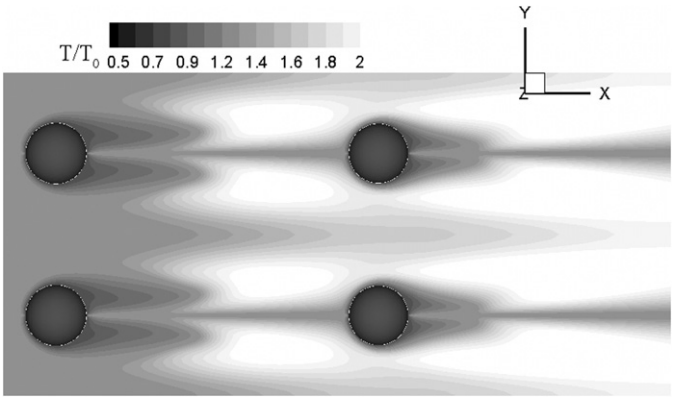

Fig. 14. Temperature contours of gas phase at 5 ms and 35% O_2 for droplet spacing with $X = 10$ and $Y = Z = 5$.

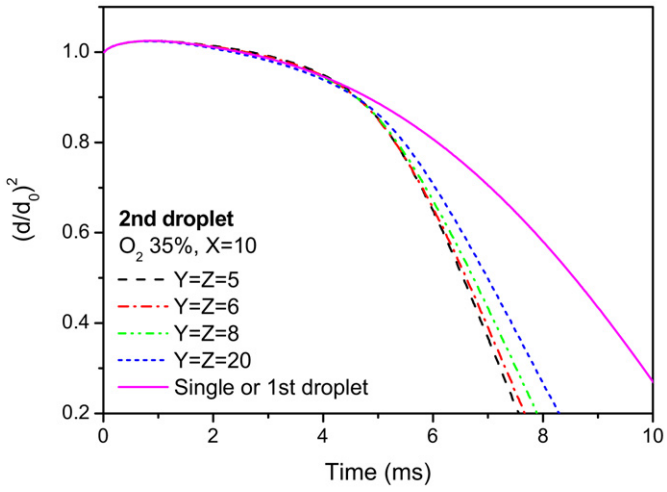

Fig. 15. Temporal variation of diameter squared of two droplets at 35% O_2 for various Y and Z with fixed $X = 10$.

In summary, the effects of convection and the merged flame are prominent when the spanwise distance is decreased at relatively low O_2 mole-fraction; i.e., 35%. In this scenario, the second droplet is greatly affected by the flame surrounding it. The first droplet, however, is hardly affected by Y and Z changes.

Figs. 16a and 16c show the flame configuration of multiple droplets for $Y = Z = 5$ and $Y = Z = 20$, respectively. The O_2 mole-fraction is set to 70% and $X = 10$. All droplets shown in Figs. 16a and 16c retain a lateral flame mode due to the high O_2 mole-fraction. The distribution obtained for $Y = Z = 5$ (see Fig. 16a) are flatter due to the flow acceleration than those obtained for $Y = Z = 20$; see Fig. 16c. Although there is no merged single flame surrounding the second droplet, the evaporation rate of the second droplet is faster for 70% O_2 mole-fraction (lifetime ending at around 6–7 ms) than that for 35% O_2 mole-fraction (lifetime ending at around 8 ms; see Fig. 15). For both first and second droplets, the trend shown in Fig. 17 is, interestingly, exactly the opposite of that shown in Fig. 15. When Y and Z are reduced, the second droplet evaporates faster at 35% than at 70% O_2 mole-fraction. Recall that at 35% O_2 mole-fraction, the flame location of the first droplet prominently affected the evaporation of the second droplet. At 70% O_2 mole-fraction, however, the first droplet flame had a minor role in this regard. Rather, the flame shape of the second droplet itself affected its own evaporation rate. As observed in Fig. 16a, the second droplet flame shape is flatter than that shown in Fig. 16c, not surrounding the entire droplet. On the other hand, when Y and Z are large, as shown

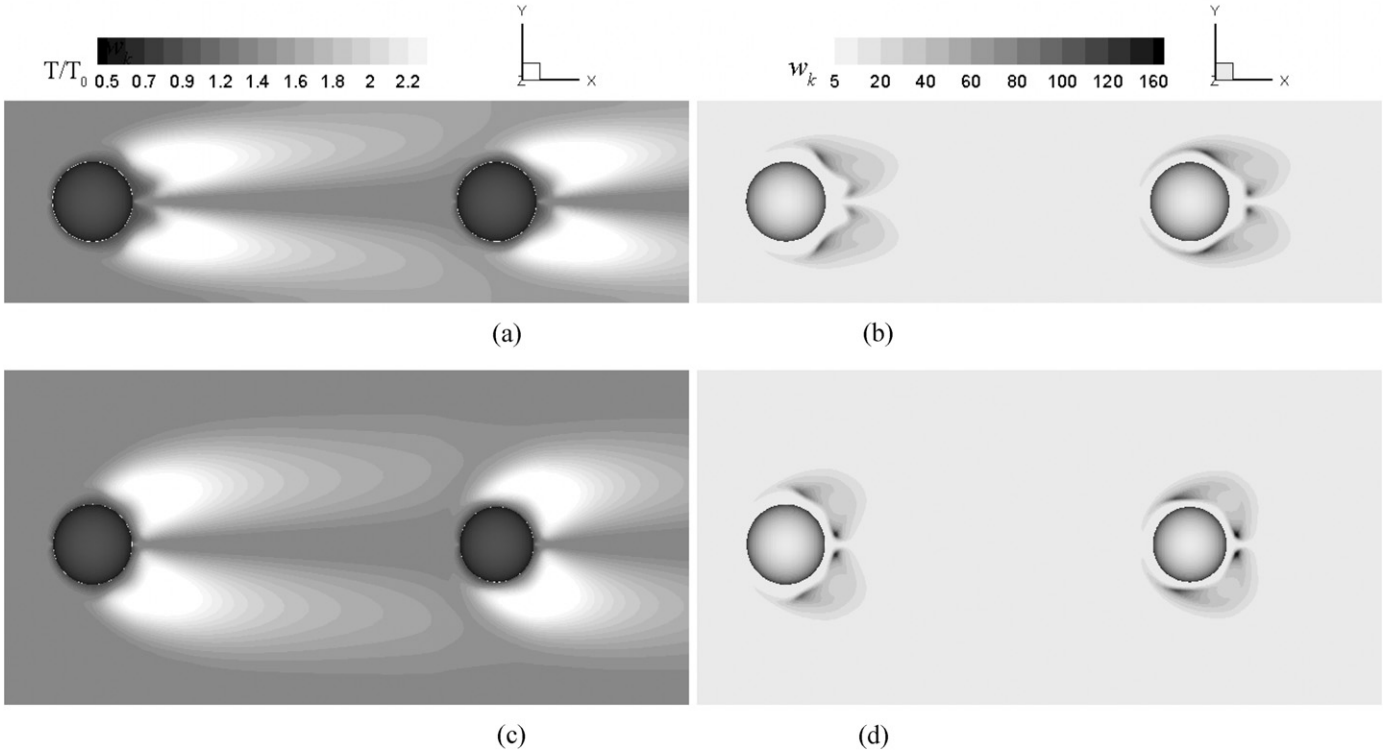

Fig. 16. Contours of gas phase at 3 ms and 70% O_2 for different Y and Z with $X = 10$: (a) temperature and (b) reaction rate (kW/m^3) contours for $Y = Z = 5$, (c) temperature and (d) reaction rate contours for $Y = Z = 20$.

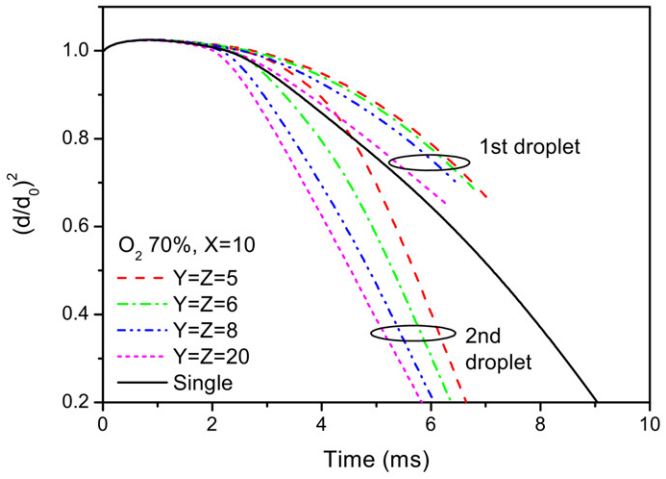

Fig. 17. Temporal variation of diameter squared of two droplets at 70% O_2 for various Y and Z with fixed $X = 10$.

in Fig. 16c, the second droplet flame covers a fairly large surface area of its own, inducing greater evaporation. The reaction rate shown in Figs. 16b and 16d further supports this explanation for the slightly larger flame coverage of the second droplet when Y and Z are increased. Note that the maximum reaction rate is located upfront of the second droplet when $Y = Z = 20$ as in Fig. 16d, but is slightly shifted downstream when $Y = Z = 5$ as in Fig. 16b. It is also worthwhile to note that the chemical reaction was computed by using an algebraic turbulent combustion model (EBU) while the rate of burning is probably governed by more complex phenomena involving turbulence-kinetics interactions. The EBU model is easier to implement, simpler to use and requires less CPU time, the reasons of which justify our choice of the EBU model.

4. Conclusions

Combustion characteristics of a three dimensional arrangement of spherical droplets at various O_2 mole-fractions in a turbulent environment were numerically investigated to examine the effects of droplet geometry on the vaporization rate of droplets. In addition, the turbulence intensity effect on the vaporization rate was also studied. Vaporization and subsequent burning of a single droplet were first calculated, and the results were verified with existing experimental data. The model then was extended to combustion of multiple droplets. Increasing turbulence intensity enhanced the turbulent mixing, which in turn expedited the vaporization and, therefore, shortened the lifetime of droplets.

As the streamwise distance was varied, it was found that four major effects were competing when the O_2 mole fraction was low (15%). First, convection-induced circulation (or Hill's vortex) caused a temporary decrease in the droplet surface temperature because of mixing inside a droplet with a low core temperature. Second, convection shielding of the second droplet by the first as well as the low temperature of its fuel vapor was also influential. Third, the wake-flame of the first droplet caused the second droplet to have a lateral flame in front of it, which in turn rapidly evaporated the second droplet. Fourth, the distance this wake-flame traveled also affected the property of the second droplet. It was also observed that the flame configuration changed from a wake-flame mode to a lateral flame mode at a higher value of the O_2 mole-fraction (50%).

As the spanwise distances (Y and Z) were varied, the second droplet evaporated faster when Y and Z were decreased under greater convection inducing rapid flame merging at the relatively low O_2 mole-fraction, 35%. However, at the 70% O_2 mole-fraction, the trend was exactly the opposite with a second droplet evaporating slower when Y and Z were reduced. In this case the first droplet flame had a minor role in influencing the second droplet

evaporation. Rather, the second droplet flame shape itself affected its own evaporation rate.

Acknowledgments

This research was supported by a Korea University Grant (2007). Special thanks is extended to Dr. Scott C. James of Sandia National Laboratories' Thermal/Fluid Science & Engineering Department and an anonymous reviewers for many helpful suggestions that improved the flow and readability of this manuscript.

References

[1] G.M. Faeth, Prog. Energy Combust. Sci. 9 (1–2) (1983) 1–76.
[2] I. Gökalp, G. Chauveau, O. Simon, X. Chesneau, Combust. Flame 89 (3-4) (1992) 286–298.
[3] N. Hiromitsu, O. Kawaguchi, Heat Transfer Jpn. Res. 24 (1995) 689–700.
[4] J.S. Wu, Y.J. Liu, H.J. Sheen, Int. J. Heat Mass Transfer 44 (24) (2001) 4593–4603.
[5] M. Birouk, I. Gökalp, Int. J. Heat Mass Transfer 45 (1) (2002) 37–45.
[6] H.Y. Kim, C.P. Cho, J.T. Chung, JSME Int. J. B 48 (2) (2005) 293–299.
[7] R. Tal, D.N. Lee, W.A. Sirignano, Int. J. Heat Mass Transfer 26 (1983) 1255–1273.
[8] R. Tal, D.N. Lee, W.A. Sirignano, Int. J. Heat Mass Transfer 27 (8) (1984) 1414–1417.
[9] M.S. Raju, W.A. Sirignano, Phys. Fluids A 2 (10) (1990) 1780–1796.
[10] C.H. Chiang, W.A. Sirignano, Atomization Sprays 3 (1) (1993) 91–107.
[11] J. Du, R.L. Axelbaum, Combust. Flame 100 (3) (1995) 367–375.
[12] K.K. Kuo, Principles of Combustion, Wiley, New York, 1986, p. 520.
[13] B.E. Poling, J.M. Prausnitz, J.P. O'Connell, The Properties of Gases and Liquids, McGraw–Hill, New York, 2001.
[14] C.K. Westbrook, F.L. Dryer, Combust. Sci. Technol. 27 (1-2) (1981) 31–43.
[15] B.F. Magnussen, B.H. Hjertager, Proc. Combust. Inst. 16 (1976) 719–729.
[16] S.R. Turns, An Introduction to Combustion, McGraw–Hill, Singapore, 2000, p. 53.
[17] C. Olikara, G.L. Borman, SAE 750468 (1975).
[18] J.P. Van Doormal, G.D. Raithby, Numer. Heat Transfer 7 (1984) 147–163.
[19] H.K. Versteeg, W. Malalasekera, An Introduction to Computational Fluid Dynamics—The Finite Volume Method, Longman Scientific & Technical, New York, 1995, p. 187.
[20] H.L. Stone, SIAM J. Numer. Anal. 5 (3) (1968) 530–558.
[21] M. Constanceau, R. Bouard, J. Fluid Mech. 79 (1977) 231–256.
[22] J.E. Rengel, S.H. Sphaier, Hybrid Methods Eng. 1 (4) (1999) 31–56.
[23] J.B.V. Wanderley, C.A. Levi, Ocean Eng. 29 (4) (2002) 445–460.
[24] S.C. Wong, A.R. Lin, J. Fluid Mech. 237 (1992) 671–687.
[25] M. Renksizbulut, M.C. Yuen, J. Heat Transfer 105 (2) (1983) 384–388.
[26] M. Renksizbulut, M.C. Yuen, J. Heat Transfer 105 (2) (1983) 389–397.